

---

# Laser Absorption, Mass Ablation Rate, and Shock Heating in Direct-Drive Inertial Confinement Fusion

## Introduction

Inertial confinement fusion (ICF) occurs when a spherical shell target containing cryogenic thermonuclear fuel (i.e., DT) is imploded.<sup>1–9</sup> The implosion is initiated by the ablation of material from the outer surface using either intense laser beams (direct drive)<sup>3,5,6,8,9</sup> or x rays produced in a high-Z enclosure (indirect drive).<sup>4,7</sup> The ablated shell mass forms a coronal plasma that surrounds the target and accelerates the shell inward via the rocket effect. When the higher-density shell converges toward the target center and is decelerated by the lower-density fuel, a hot spot forms. Compression by the cold, dense shell causes the pressure and DT fusion reaction rate of the hot spot to increase. It is predicted that the  $\alpha$ -particle fusion products will deposit sufficient energy in the hot spot to launch a thermonuclear burn wave out through the cold, dense fuel in the shell just prior to stagnation when the areal density of the hot spot exceeds  $0.3 \text{ g/cm}^2$  and the hot-spot temperature reaches 10 keV (Ref. 4). Energy gain with hot-spot ignition depends on the implosion velocity of the shell  $V_{\text{imp}}$ , the shell areal density  $\rho R_{\text{shell}}$  at the time of burn, and the in-flight shell adiabat  $\alpha = P_{\text{fuel}}/P_{\text{Fermi}}$ , defined as the ratio of the pressure in the main fuel layer  $P_{\text{fuel}}$  to the Fermi-degenerate pressure  $P_{\text{Fermi}}$ .<sup>4,10–12</sup>

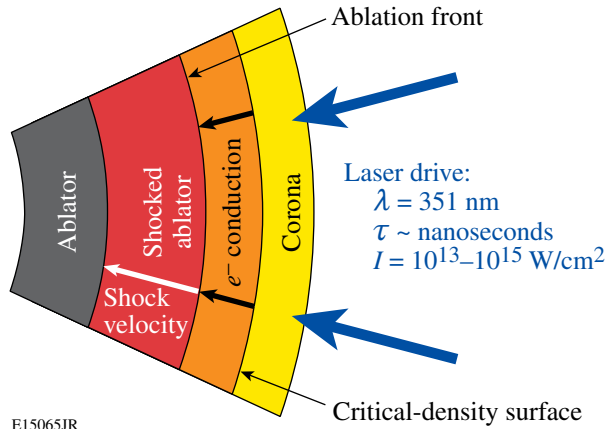
A physical understanding of the energy transport from the laser to the target is required to develop capsule designs that can achieve energy gain with ICF. An experimental investigation of direct-drive energy coupling is the subject of this article. The 60-beam, 30-kJ, 351-nm OMEGA Laser System<sup>13</sup> is used to irradiate millimeter-scale, spherical and planar plastic and cryogenic  $\text{D}_2$  and DT targets on nanosecond time scales with peak intensities  $I$  ranging from  $10^{13}$  to  $10^{15} \text{ W/cm}^2$ . High levels of laser drive uniformity are achieved with 2-D smoothing by spectral dispersion (SSD) and polarization smoothing (PS).<sup>14</sup> The three major parts of energy coupling—laser absorption, electron thermal transport, and shock heating of the target—were diagnosed with a wide variety of experiments. The experimental results are compared with the simulations of the 1-D hydrodynamics code *LILAC*,<sup>15</sup> which is used to design ignition targets for the 1.8-MJ, 351-nm, 192-beam National Ignition Facility (NIF).<sup>16</sup> The initial design of a direct-drive-ignition target relies on 1-D simulations

to optimize the energetics of the implosion. Subsequent calculations are performed with the 2-D hydrodynamics code *DRACO* to mitigate the deleterious effects of hydrodynamic instabilities on target performance.<sup>17</sup> Energy coupling to the target is primarily a 1-D effect; therefore, comparisons of experimental results with 1-D *LILAC* simulations are presented. The physics of direct-drive energy coupling is similar for plastic and cryogenic targets. The initial coupling is identical since cryogenic targets have a thin plastic ablator; however, the subsequently formed lower-Z, hydrogen-isotope, coronal plasma absorbs less laser energy. Plastic targets reduce the complexity and cost of the experiment and increase the shot rate.

ICF target acceleration and deceleration are realized when hot, low-density plasma pushes against cold, high-density plasma, making the target implosion inherently susceptible to the Rayleigh–Taylor (RT) hydrodynamic instability.<sup>4–9,18–20</sup> High-gain, direct-drive ICF target implosions require accurate predictions of the shell adiabat  $\alpha$  since it defines the minimum energy needed for hot-spot ignition and the amount of ablative stabilization in the RT growth rate. The shell adiabat is tuned by varying the temporal pulse shape of the laser irradiation. The minimum energy for hot-spot ignition scales as  $E_{\text{min}} \propto (\alpha^{1.8}/V_{\text{imp}}^{5.8})$  (Refs. 11 and 12); hence, low-adiabat implosions with high-implosion velocities require less laser energy to ignite. A higher adiabat at the ablation front reduces the RT growth rate  $\gamma_{\text{RT}} = \alpha_{\text{RT}} \sqrt{k g} - \beta_{\text{RT}} V_a$ , where  $\alpha_{\text{RT}}$  and  $\beta_{\text{RT}}$  are constants,  $k$  is the wave number of the perturbation, and  $g$  is the target acceleration (Refs. 18 and 19), by increasing the ablative stabilization term,<sup>21,22</sup> which is proportional to the velocity of the ablation front with respect to the unablated shell  $V_a$ . The ablation velocity depends on the shell adiabat  $V_a \propto \alpha^{3/5}$  (Ref. 19). A balance must be struck between the laser energy and the shell stability constraints to choose a shell adiabat.

A schematic of direct-drive energy coupling is presented in Fig. 109.1. After the initial breakdown of the target surface with the intense laser beams, the laser light no longer propagates to the ablation front. Instead, the expanding coronal plasma forms a critical electron density  $n_{\text{cr}} = \pi m c^2 / e^2 \lambda_L^2$ , where  $m$  is the

electron mass,  $c$  is the speed of light,  $e$  is the electron charge, and  $\lambda_L$  is the laser wavelength, and the laser energy is absorbed primarily via inverse bremsstrahlung in the underdense corona having electron densities less than the critical density  $n_e \leq n_{cr}$ , where  $n_{cr}(\lambda_L = 351 \text{ nm}) = 9 \times 10^{21} \text{ cm}^{-3}$ . The fraction of laser energy absorbed in the corona,  $f_{abs}$ , is inferred from measurements of the scattered light.



EI5065JR

Figure 109.1

Diagram illustrating the flow of energy from the laser to the target in direct-drive ICF. Typical laser irradiation conditions are listed. The laser energy is absorbed in the corona at densities less than the critical density via inverse bremsstrahlung. Thermal electron conduction transports the absorbed energy to the ablation front. Laser ablation launches a shock wave in the ablator or shell of the target.

As shown in Fig. 109.1, the energy flows from the critical-density surface to the ablation front via electron thermal transport. This process is calculated in *LILAC*<sup>15</sup> using a flux-limited thermal transport model.<sup>23</sup> The efficiency  $\eta_{hydro}$  of this process can be obtained by comparing the mass ablation rate  $\dot{m}$  to the measured laser absorption fraction  $f_{abs}$ .<sup>4</sup> The mass ablation rate is inferred from time-resolved x-ray burnthrough measurements of laser-driven targets with buried high- $Z$  tracer layers.<sup>24–34</sup> To eliminate the early burnthrough due to the RT instability growth,<sup>34</sup> the measurements are performed on solid, plastic spherical targets. In contrast to an accelerating, spherical shell target with a buried high- $Z$  layer, a solid target does not accelerate and is not susceptible to the RT instability; therefore, the burnthrough measurement will be affected only by the laser ablation. The effects of the Richtmyer–Meshkov instability on the burnthrough experiments presented here have been estimated to be negligible. Both the ablation pressure  $P$  and the mass ablation rate depend on the amount of energy coupled to the ablation front:  $P \propto (f_{abs}\eta_{hydro}I)^{2/3}$  and  $\dot{m} \propto (f_{abs}\eta_{hydro}I)^{1/3}$ , and the implosion velocity is proportional to the ratio of the ablation pressure to the mass ablation rate  $V_{imp} \propto (P/\dot{m})$  (Ref. 4).

The laser ablation process launches a shock wave into the target that compresses and heats the shell (Fig. 109.1). This primary source of heating determines the adiabat for the bulk of the shell. X-ray radiation and energetic electrons provide additional but lower levels of shell heating. Diagnosing the plasma conditions in the shock-heated shell and modeling its equation of state are challenging since they straddle the boundaries between Fermi-degenerate, strongly coupled, and weakly coupled plasmas (i.e.,  $10^{23} \text{ cm}^{-3} < n_e < 10^{24} \text{ cm}^{-3}$  and  $10 \text{ eV} < T_e < 40 \text{ eV}$ ). Such plasmas are too cold to emit x rays and too dense to be probed with optical Thomson scattering. The amount of shock heating in planar-CH-foil targets was diagnosed with time-resolved x-ray absorption spectroscopy<sup>35–37</sup> and noncollective spectrally resolved x-ray scattering.<sup>38</sup>

The implosion can be divided into four stages: shock propagation, acceleration phase, deceleration phase, and peak compression. This article concentrates on the first two stages, when the laser irradiates the target and when the shell adiabat is set. It is organized as follows: A description of the 1-D hydrodynamics code and its predictions are presented in **1-D Hydrodynamics Code** (p. 2). The scattered-light measurements are presented in **Laser-Absorption Experiment** (p. 3). The laser-driven burnthrough measurements are described in **Mass-Ablation-Rate Experiment** (p. 5). The shock-heating measurements are presented in **Shock-Heating Experiment** (p. 8). Throughout this article, the highly reproducible experimental results achieved with a high level of laser drive uniformity are shown to constrain the modeling of direct-drive energy transport from the laser to the target. The limitations of the flux-limited thermal-transport model<sup>23</sup> and further improvements in the modeling are presented in **Discussion** (p. 11). A nonlocal treatment of the thermal transport, which is in progress,<sup>39</sup> is expected to improve agreement between the simulation and the experiment.

### 1-D Hydrodynamics Code

Direct-drive implosions on the OMEGA Laser System are routinely simulated with the 1-D hydrodynamics code *LILAC*.<sup>15</sup> This code is used to design high-gain, direct-drive implosions for the NIF.<sup>6,8,9</sup> The electron thermal conduction that throttles the energy flow in direct-drive ICF is challenging to model.<sup>23,39,40</sup> As described below, it is currently simulated with a flux-limited thermal-transport model. The main objective of this detailed investigation is to tune the physics models in *LILAC* by comparing the predicted laser absorption, mass ablation rate, and shock heating with the measured quantities. Accurate simulations of OMEGA experiments will instill confidence in the target designs for the NIF.

A detailed description of *LILAC* can be found elsewhere<sup>15</sup> with the main features of the code described in this section. Laser absorption is calculated using a ray-trace algorithm that models inverse bremsstrahlung. Transport of radiation is modeled through multigroup diffusion with the Los Alamos National Laboratory Astrophysical Tables<sup>41</sup> providing the opacities. The *SESAME* tables are used to model the equation of state. *LILAC* uses a flux-limited Spitzer–Härm<sup>42</sup> electron-thermal-conduction model that calculates the effective heat flux  $q_{\text{eff}}$  using a sharp cutoff model [i.e.,  $q_{\text{eff}} = \min(q_{\text{SH}}, f q_{\text{FS}})$ ]. The heat flux is proportional to the temperature gradient  $q_{\text{SH}} = -\kappa \nabla T_e$ . In the region where  $q_{\text{SH}} > q_{\text{FS}}$ , the heat flux is calculated as a fraction  $f$  of the free stream limit  $q_{\text{FS}} = n T_e V_T$ , where  $\kappa$  is the heat conductivity,  $T_e$  is the electron temperature,  $V_T = \sqrt{T_e/m_e}$  is the thermal electron velocity, and  $n_e$  is the electron density. The coefficient  $f$  is commonly referred to as a “flux limiter.” Typical values of  $f$  for simulations of direct-drive experiments are  $0.04 < f < 0.1$ . The larger the flux limiter, the closer the heat flux is to the classical Spitzer–Härm limit.

The classical heat-transport theory of Spitzer–Härm is valid when the mean free path of the electron is much smaller than the temperature-gradient length of the plasma. This is not a

good approximation for the steep gradients near the critical density in direct-drive ICF. Nonlocal energy-transport calculations have been proposed using Fökker–Planck codes to model the heat flux in direct-drive ICF when the temperature scale length is a few electron mean free paths;<sup>40</sup> however, until recently such calculations have been implemented with limited success in hydrodynamics codes.<sup>43</sup> A new nonlocal-transport model using a simplified Boltzmann equation (Krook model) has been developed and incorporated in *LILAC*.<sup>39</sup>

**Laser-Absorption Experiment**

The fraction of laser energy absorbed in the corona is inferred from power measurements of the 351-nm light scattered from spherical implosions<sup>44–47</sup> of cryogenic D<sub>2</sub> and plastic-shell targets.<sup>48</sup> Scattered light is detected behind two focusing lenses in the full-aperture backscatter stations (FABS) of beams 25 and 30: time-resolved spectra and calorimetric measurements are recorded.<sup>49</sup> Time-resolved spectra of the scattered light collected between the focusing lenses are also recorded. The scattered light is assumed to be distributed uniformly over  $4\pi$  since the calculated deviations from isotropy are in the 1% to 2% range. As shown in Fig. 109.2, there is good agreement (within  $\pm 2\%$  rms) between time-integrated

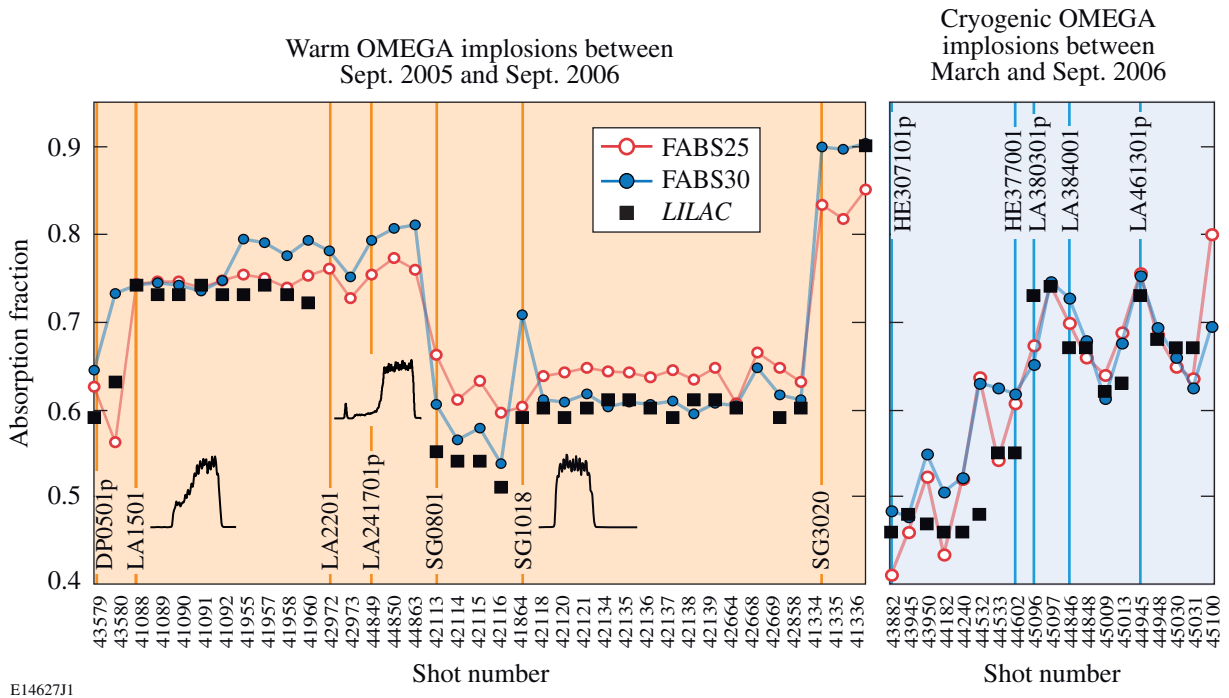


Figure 109.2 Time-integrated laser-absorption fraction measured on OMEGA for a variety of targets, laser pulse shapes, and irradiation energies. Good agreement is observed between the *LILAC* prediction (square symbols) and the measurements recorded in beams 25 and 30 (circle symbols) with the full-aperture backscatter stations (FABS25 and FABS30).

absorption data and the *LILAC* predictions for a wide variety of targets, laser pulse shapes, and irradiation energies. (The overall accuracy of the FABS calorimetry is estimated at 1% to 2% rms. Systematic errors of  $\leq 3\%$  between the calorimeters in the two FABS stations arise from the shot-to-shot variations in the transmissions of the blast shields protecting the OMEGA focus lenses that are coated with target debris from experiments. These errors are calibrated and corrected during routine system maintenance every few weeks.)

Since the shell adiabat is tuned by varying the temporal pulse shape of the laser irradiation, power measurements of the scattered light are essential to characterize the drive. The time-resolved scattered-light spectrum presented in Fig. 109.3(a) was recorded for the shaped laser pulse drive shown on a linear scale in Fig. 109.3(a) and a log scale in Fig. 109.3(b). The laser pulse has a low-intensity foot followed by a higher-intensity main drive. The shell adiabat is set during the foot portion of the pulse. A comparison of the time histories of the measured, spectrally integrated, scattered-light signal and the *LILAC* prediction is shown in Fig. 109.3(b). Two flux limiters were considered:  $f = 0.06$  and  $f = 0.1$ . Overall the *LILAC* prediction for the scattered-light power is in good agreement with the measurement over more than three orders of magnitude; however, some differences (10% of the absolute scattered-light fraction) are observed that could affect the shock dynamics

(i.e., shock timing and shock strength). It is difficult to ascribe a single rms error estimate to the time-resolved absorption (or scattered-light) measurements. The absorption and scattering processes are affected by detailed coronal plasma conditions created by the incident laser pulse shape. During the first 100 ps of the laser pulse and at low intensities, the discrepancy can be as high as 50% or more without affecting the time-integrated absorption, while later in the plasma evolution, nonlinear effects can instantaneously lead to enhanced scattering of up to 10%. These discrepancies are well outside the experimental error bars, which depend on the dynamic range and the recording intensities on the streak camera. The discrepancy revealed with the scattered-light power is not evident in shock-velocity measurements, which can discriminate between the flux limiters under consideration.<sup>39,50</sup>

The measured absorption is systematically higher than predicted during the first 100 to 200 ps of the laser pulse. This is difficult to see in Fig. 109.3(b) because of the compressed time scale. The higher absorption at early times during the initial plasma formation is more apparent with a double-picket laser pulse (i.e., a train of two 100-ps laser pulses separated by 400 ps with  $\sim 12$  J/beam in the first pulse and  $\sim 18$  J/beam in the second pulse) experiment. The double-picket laser pulse shape is presented in Fig. 109.4(a), with the resulting streaked spectrum of the measured scattered light shown in Fig. 109.4(b).

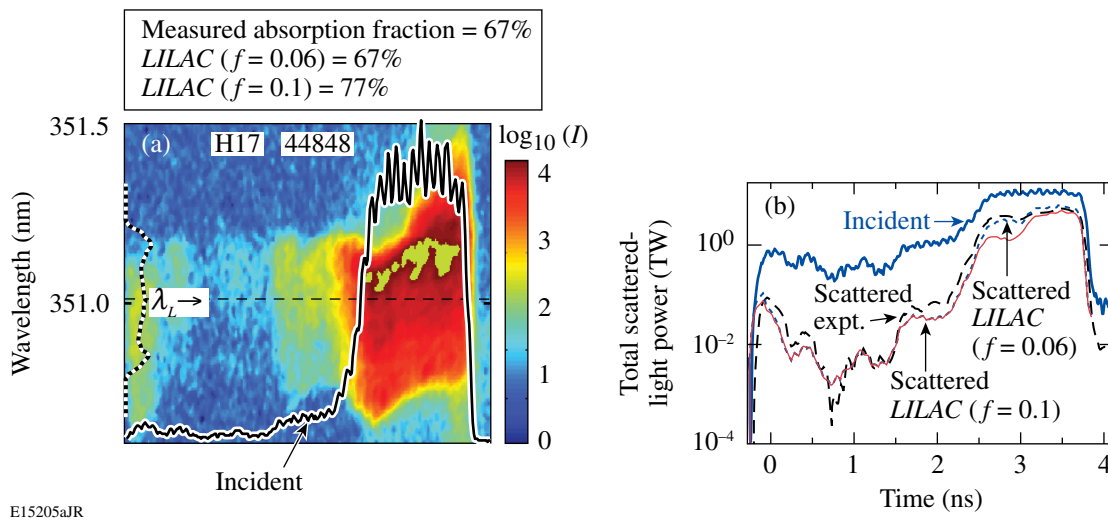


Figure 109.3

(a) Time-resolved spectral measurement of 351-nm scattered laser light for a shaped laser pulse irradiating a spherical DT cryogenic implosion target having a 95- $\mu\text{m}$ -thick cryogenic DT layer inside a 5.4- $\mu\text{m}$ -thick CD shell. The incident pulse shape (solid curve) and the broad incident spectrum (dotted curve) are overplotted on linear scales. (b) Spectrally integrated power measurement of scattered laser light (dashed curve) recorded with a laser pulse shape (bold solid curve) incident on target. *LILAC* predictions for two flux limiters are shown:  $f = 0.06$  (dotted curve) and  $f = 0.1$  (solid curve). Time-integrated laser absorption fractions are listed for the three scattered-light curves.

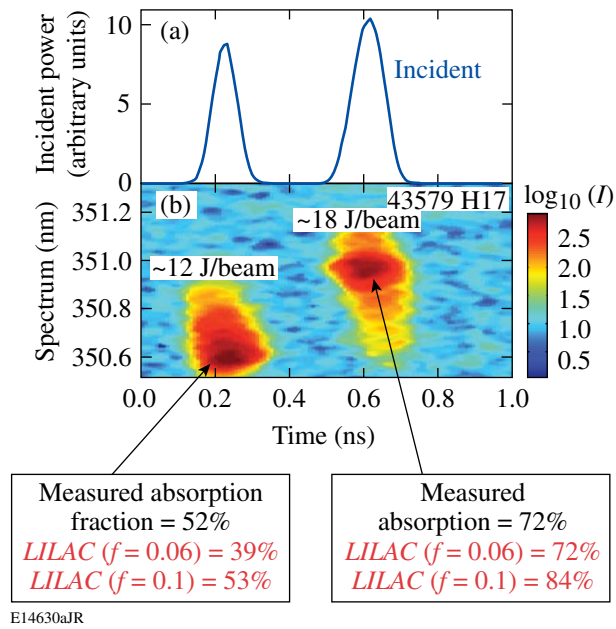


Figure 109.4

(a) Intensity of double-picket laser pulse shape irradiating a spherical plastic target, and (b) associated time-resolved, spectral measurement of scattered laser light. Measured time-integrated laser absorption fractions are listed for the two 100-ps picket pulses and compared with the *LILAC* predictions for two flux limiters ( $f=0.06$  and  $f=0.1$ ). The first pulse has  $\sim 12$  J/beam and the second pulse has  $\sim 18$  J/beam.

Although the 52% temporally integrated absorption fraction inferred from the experiment for the first peak is higher than the 39% *LILAC* prediction with  $f=0.06$ , a simulation with a higher flux limiter of  $f=0.1$  (predicted absorption fraction = 53%) matches the experimental result. After the corona is established with the first pulse, the measured absorption fraction of the second pulse (72%) is matched with the lower flux limiter (predicted absorption fraction = 72%), while the higher flux limiter of  $f=0.1$  overpredicts an absorption fraction of 84%. Therefore, the flux limiter needs to vary in time to simulate the measured absorption fraction. Fökker–Planck simulations have predicted a time-varying flux limiter.<sup>43</sup> The enhanced absorption at early times is likely due to resonance absorption at very low  $I\lambda_L^2 < 10^{13}$  W $\mu\text{m}^2/\text{cm}^2$  with concomitant low energetic electron production ( $T_h < 10$  keV). In the overall energetics this enhanced absorption is negligible; however, the energetic electrons can deposit their energy in the shell.

The time-resolved scattered-light spectra shown in Figs. 109.3(a) and 109.4(b) contain significant information. The initial rapid blue shift in the spectra is directly related to the rapid buildup of the plasma corona whose optical path length decreases as the plasma size increases. This is most easily

seen in Fig. 109.4(b) where the incident laser bandwidth was very narrow compared to the scattered-light spectra shown. In addition, the broad incident spectrum presented in Fig. 109.3(a) (dotted line) changes dramatically during the high-intensity part of the laser pulse, indicating that nonlinear processes are changing the spectra and possibly the scattered-light levels. A detailed investigation of these spectra is currently underway.

### Mass-Ablation-Rate Experiment

The mass ablation rate is inferred from time-resolved x-ray burnthrough measurements<sup>24–34</sup> of solid, spherical plastic targets with buried tracer layers of Ti. Hydrodynamic instabilities are expected to have negligible effects on the inferred mass ablation rate since these targets do not accelerate. The 1-D simulations show that the shell trajectory of an imploding target has a negligible effect on the mass ablation rate for the 1-ns square laser pulse; therefore, the non-accelerating, solid, spherical burnthrough target is predicted to have a mass ablation rate similar to the shell target. The target shown in Fig. 109.5 is irradiated with 60 beams smoothed with 2-D SSD and PS,<sup>14</sup> using a 23-kJ, 1-ns square laser pulse with a peak intensity of  $1 \times 10^{15}$  W/cm<sup>2</sup>. The ablation time is measured for three ablator thicknesses (2, 5, and 8  $\mu\text{m}$ ) to sample the mass ablation rate at different times during the laser pulse. It is predicted that the mass ablation rate for the 1-ns square laser pulse, having near-constant laser irradiation, has small temporal variations; therefore, the burnthrough experiment is not preferentially sampling particular times during the laser pulse. The mass ablation rate is inferred from the onset of the K-shell emission of the ablated Ti tracer layer. Prior to ablation the Ti layer is too cold to emit x rays; however, as the Ti is ablated into the hot corona, a significant fraction of

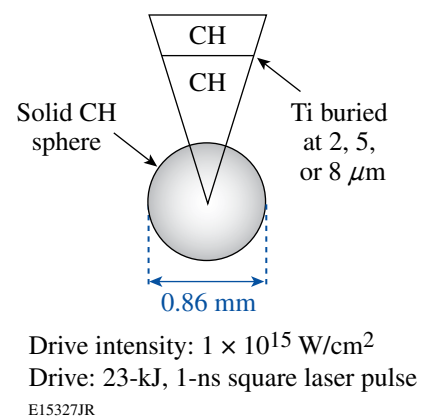


Figure 109.5

Diagram of nonaccelerating target used for laser-driven burnthrough experiment. The solid, spherical plastic (CH) target has a buried tracer layer of Ti (0.1  $\mu\text{m}$  thick). The target specifications and laser irradiation conditions are shown.

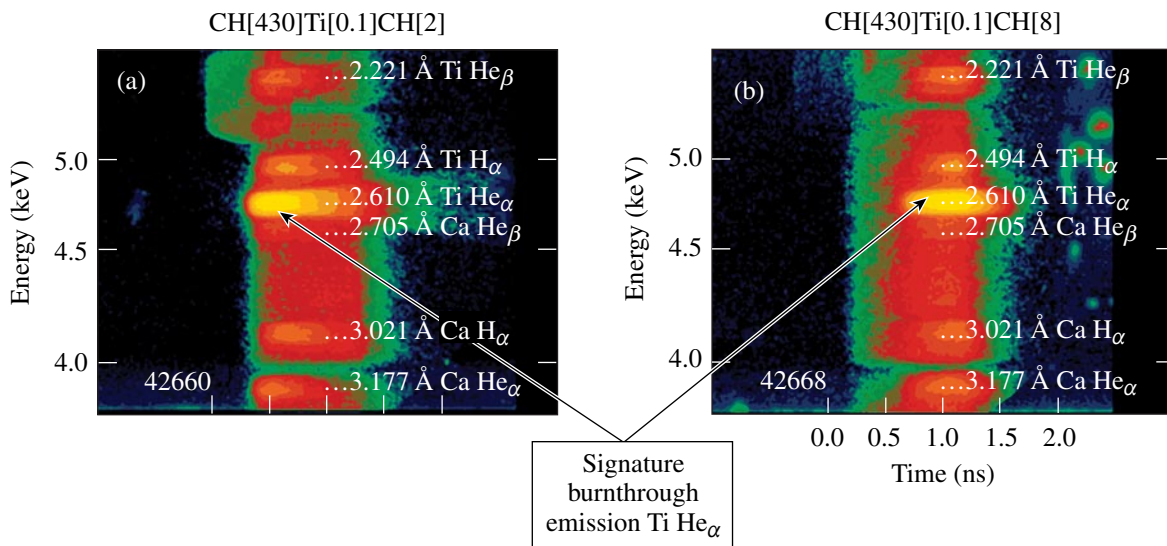
its population is ionized to the He-like and H-like charge states and emits K-shell emission in the 4.5- to 5.5-keV photon energy range. The experimental signature of burnthrough is given by the Ti He $_{\alpha}$  emission.

Time-resolved, Ti K-shell spectroscopic measurements were performed with x-ray streak cameras<sup>51</sup> outfitted with a Bragg crystal spectrometer that used a flat RbAP (rubidium acid phthalate) crystal to disperse the spectrum onto a gold photocathode. The time axis for the streaked x-ray spectra was established as follows: The streak speed of the camera is calibrated using a temporally modulated ultraviolet laser pulse (i.e., a sequence of eight consecutive Gaussian laser pulses having a 548-ps period). The temporal resolution, defined by the streak speed and the photocathode slit width, is 50 ps. Defining the time  $t = 0$  is challenging because the initial x-ray emission from the target is below the detection threshold of the diagnostic. Using the 4.5-keV x-ray continuum emission as a timing fiducial, the absolute timing is determined by synchronizing the measured pulse with the simulated one as described below. The synchronization is performed for each flux limiter under consideration since the temporal shape of the x-ray pulse depends on the flux limiter. The standard deviation of the difference between the measured and simulated x-ray pulse duration is 50 ps; therefore, the uncertainty in the measured burnthrough time is estimated to be  $\pm 50$  ps. The spectra

recorded for the 2- $\mu\text{m}$  CH ablator are shown in Fig. 109.6(a). The laser strikes the target at  $t = 0$  ns and the onset of the Ti He $_{\alpha}$  signature burnthrough emission occurs around 0.3 ns. A similar measurement is presented in Fig. 109.6(b) for the 8- $\mu\text{m}$  CH ablator. The spectral resolving power ( $E/\Delta E \sim 50$ ) is limited by source broadening but is clearly high enough to resolve the prominent Ti K-shell emissions. The streaked spectra presented in Fig. 109.6 show that the burnthrough occurs later for the target with the thicker CH ablator, as expected.

Weak Ca K-shell emissions are observed in the burnthrough x-ray spectra of Fig. 109.6. Calcium is a surface contaminant of the solid plastic target introduced during production of the sphere. The calcium layer is ablated into the coronal plasma and emits K-shell emission around the same time as Ti. It is an experimental artifact that does not affect the measured burnthrough time.

The x-ray emission from the corona is simulated by post-processing the *LILAC* prediction with the time-dependent atomic physics code *Spect3D*.<sup>52</sup> As mentioned above, the x-ray continuum emission from the target during the first few hundred picoseconds is below the detection threshold of the diagnostic; therefore, the absolute timing of the measurement is established by synchronizing the measured x-ray continuum in the 4.5-keV range with the *LILAC/Spect3D* prediction. The



E15067JR

Figure 109.6

(a) Streaked x-ray spectrum recorded on a laser-driven burnthrough experiment with the prominent Ti K-shell emissions identified for the 2- $\mu\text{m}$ -thick CH ablator. The mass ablation rate is inferred from the signature Ti He $_{\alpha}$  emission. (b) Streaked x-ray spectrum for the 8- $\mu\text{m}$ -thick CH ablator. Calcium is a surface contaminant of the solid plastic target introduced during production of the sphere. The calcium layer is ablated into the coronal plasma and emits K-shell emission around the same time as Ti.

synchronized x-ray pulses are shown in Fig. 109.7(a) for the 8- $\mu\text{m}$  CH ablator. In Fig. 109.7(b), the temporal evolution of the Ti He $_{\alpha}$  emission predicted with *LILAC/Spect3D* is compared with the measured burnthrough emission for the 8- $\mu\text{m}$  CH ablator. Two flux limiters ( $f=0.06$  and  $f=0.1$ ) were considered, and the experimental results are closer to the predictions with the higher flux-limiter value. Comparisons of the predicted

and measured burnthrough times for these two flux limiters are presented in Fig. 109.8 for the ablators under consideration. The burnthrough time is defined as the time at which the Ti He $_{\alpha}$  emission reaches 10% of its peak intensity. It is clear from Fig. 109.8 that the burnthrough experiment is more consistent with the higher mass ablation rate of the *LILAC* prediction with  $f=0.1$ . A flux limiter of  $f=0.1$  was also needed to simulate the

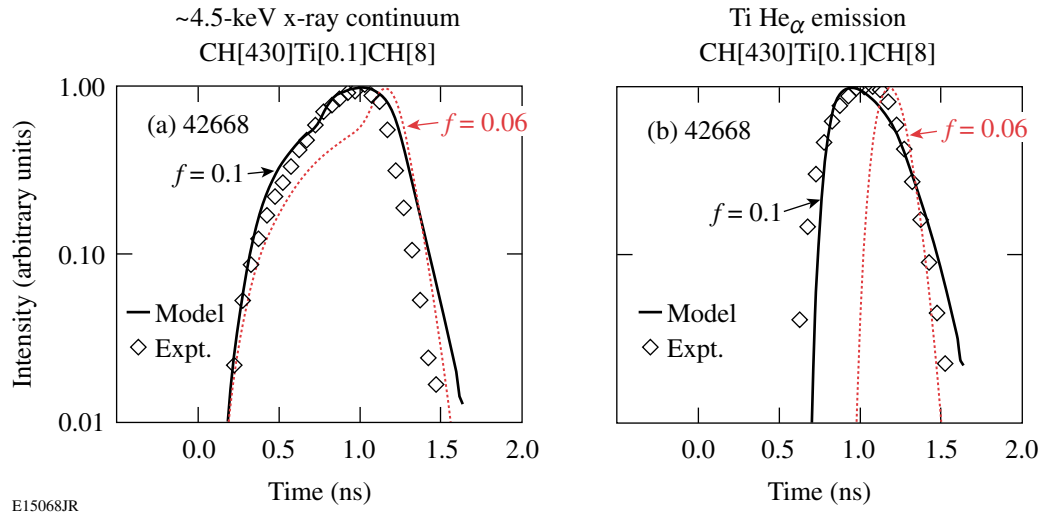


Figure 109.7 (a) Time histories of the measured (diamond symbols) and simulated (dotted curve for  $f=0.06$  and solid curve for  $f=0.1$ ) x-ray continuum in the ~4.5-keV range, and (b) time histories of the measured (diamond symbols) and simulated (dotted curve for  $f=0.06$  and solid curve for  $f=0.1$ ) Ti He $_{\alpha}$  emission for the laser-driven burnthrough experiment.

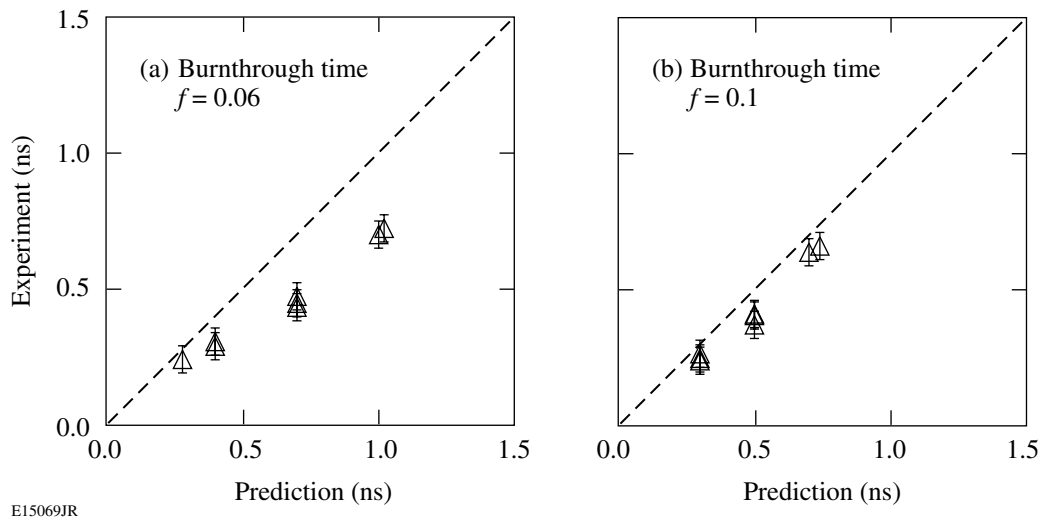


Figure 109.8 A comparison of the measured laser-driven burnthrough time and (a) the *LILAC* prediction with a flux limiter  $f=0.06$  and (b) the *LILAC* prediction with a flux limiter  $f=0.1$  for the three ablators under consideration.

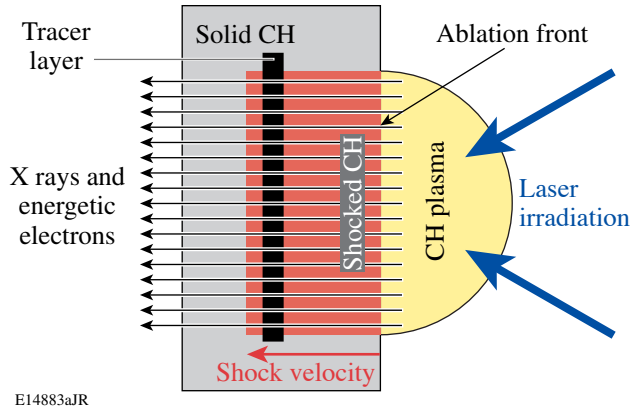
ablation-front perturbation oscillations for Richtmyer–Meshkov instability experiments on OMEGA.<sup>39,53</sup>

**Shock-Heating Experiment**

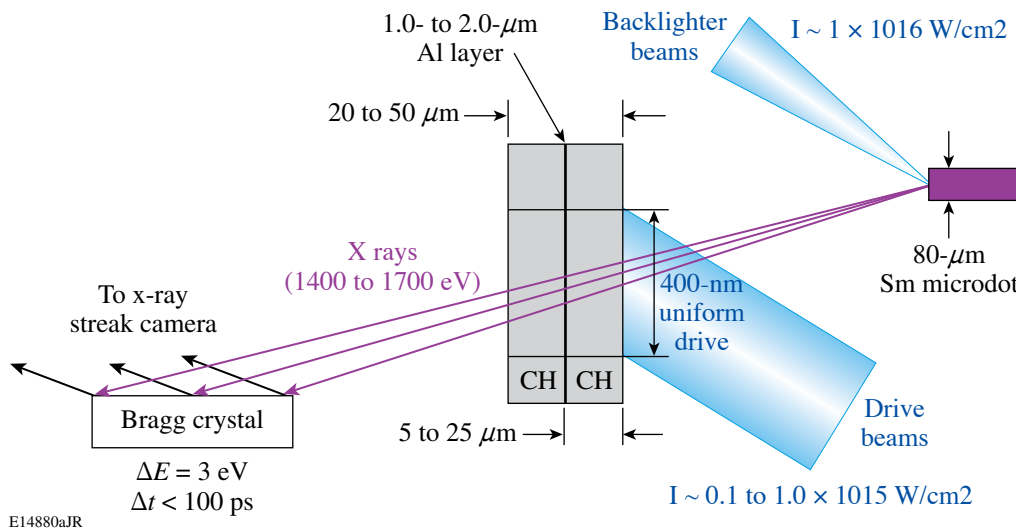
The shock wave launched by laser ablation into the target is the primary source of heating for the bulk of the shell. X-ray radiation and energetic electrons from the corona can provide additional heating to portions of the shell near the ablation front. The amount of shock heating in planar-CH-foil targets was diagnosed using two techniques: time-resolved x-ray absorption spectroscopy and noncollective spectrally resolved x-ray scattering. A detailed description of the latter experiment can be found elsewhere.<sup>38</sup> The results of the former experiment will be briefly described in this section; however, a more detailed version will be published separately.<sup>37</sup> Planar geometry is a good approximation for the shell during the shock-propagation stage of the implosion since convergence can be neglected. It also provides better diagnostic access than a spherical shell target.

Local shell conditions were measured using time-resolved x-ray absorption spectroscopy of plastic foil targets with a buried tracer layer of Al as shown in Fig. 109.9. As the shock wave propagates through the Al, it compresses and ionizes the Al. The buried depth of the tracer layer is varied to probe the plasma conditions in different regions of the target. As shown in Fig. 109.10, Al *1s–2p* x-ray absorption spectroscopy of a CH planar target with a buried Al tracer layer (1 to 2 μm thick) was performed with a point-source (i.e., <100-μm) Sm backlighter irradiated with laser intensities of ~10<sup>16</sup> W/cm<sup>2</sup>. The overall

thickness (~50 μm) of the drive foil was chosen to delay the acceleration phase until after the absorption spectra were recorded, minimizing the influences of hydrodynamic instabilities on the measurements. The direct-drive target was irradiated with up to 18 laser beams that were smoothed with phase plates, 2-D SSD, and PS.<sup>14</sup> The overlapped intensity had a uniform drive portion with a 400-μm diameter and peak intensities in the range of 10<sup>14</sup> to 10<sup>15</sup> W/cm<sup>2</sup>. The Sm M-shell emission in the 1.4- to 1.7-keV range overlaps the bound–bound absorption features of Al near 1.5 keV and probes the uniform drive portion of the target.<sup>35</sup>



E14883aJR  
Figure 109.9  
Diagram of the target used to diagnose the shock-heated conditions of a direct-drive ICF target. X-ray radiation and energetic electrons provide additional heating. X-ray absorption spectra of buried high-Z tracer layer are used to diagnose the plasma conditions in the shock-heated target. The position of the layer is varied to probe different regions of the target.



E14880aJR  
Figure 109.10  
Layout of the Al *1s–2p* absorption-spectroscopy experiment showing the Sm backlighter, the plastic drive foil with the buried Al layer, and the Bragg crystal spectrometer.

The frequency-dependent transmission of the shock-heated Al layer, obtained from the ratio  $I(\nu)/I_0(\nu) = e^{-\mu(\nu, n_e, T_e)\rho\Delta L}$  of the transmitted backlighter spectrum  $I(\nu)$  to the incident Sm spectrum  $I_0(\nu)$ , depends on the mass absorption coefficient  $\mu$  and the areal density of the Al layer  $\rho\Delta L$ . The absorption coefficient is sensitive to variations in  $n_e$  and  $T_e$  for the shock-heated conditions under consideration.<sup>36</sup> The high electron densities cause the spectral line shapes of the bound-bound absorption features to be Stark-broadened beyond the instrumental spectral resolution ( $\sim 3$  eV). The incident and transmitted spectra were recorded with an x-ray streak camera<sup>51</sup> outfitted with a Bragg crystal spectrometer that used a flat RbAP crystal to disperse the spectrum onto a low-density CsI photocathode. The temporal resolution of the measurement was  $\sim 100$  ps.

The sensitivity of the absorption spectroscopy to variations in the electron temperature is illustrated in Fig. 109.11. The predicted Al  $1s-2p$  absorption spectra, obtained by post-processing the *LILAC* simulation for shot #44116 with the time-dependent atomic physics code *Spect3D*,<sup>52</sup> are compared to the electron temperature in the Al layer. The target had a  $1\text{-}\mu\text{m}$ -thick Al layer buried at a depth of  $10\text{ }\mu\text{m}$  in a  $50\text{-}\mu\text{m}$ -thick CH target and was irradiated with a 1-ns square laser pulse having a peak intensity of  $1 \times 10^{15}$  W/cm<sup>2</sup>. A flux limiter of 0.06 was used for the simulation. The electron temperature in the Al layer was calculated as follows: The *LILAC/Spect3D* spectra

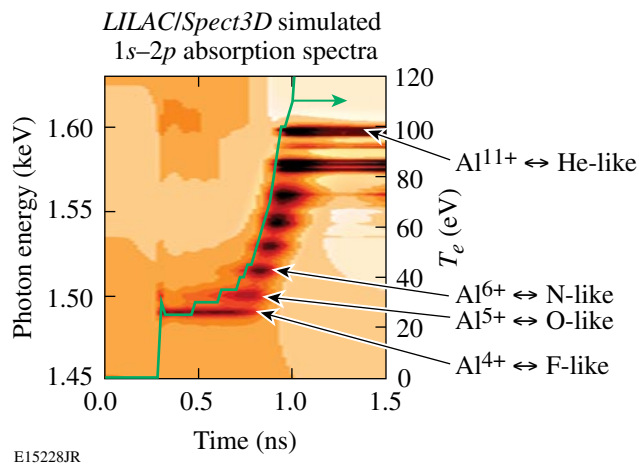


Figure 109.11

Temporal evolution of the Al  $1s-2p$  absorption spectrum simulated with *LILAC* using  $f = 0.06$  and *Spect3D* for shot #44116. The target had a  $1\text{-}\mu\text{m}$ -thick Al layer buried at a depth of  $10\text{ }\mu\text{m}$  in a  $50\text{-}\mu\text{m}$ -thick CH target and was irradiated with a 1-ns square laser pulse having a peak intensity of  $1 \times 10^{15}$  W/cm<sup>2</sup>. The predicted electron temperature in the Al layer is also plotted (solid curve). Higher-charge states of Al are ionized in succession and absorb in  $1s-2p$  transitions as  $T_e$  increases.

were compared with spectra calculated with the time-dependent atomic physics code PrismSPECT<sup>52</sup> assuming uniform shell conditions for various combinations of  $n_e$  and  $T_e$ . The best fit between the *LILAC/Spect3D* spectra and PrismSPECT was determined based on a least-squares-fitting routine, which inferred  $n_e$  and  $T_e$  simultaneously. The accuracy of the  $T_e$  inference is 10%, while the uncertainty of the  $n_e$  inference is about a factor of 2. The stair step in the simulated electron temperature observed in Fig. 109.11 around 0.5 ns is due to the discrete electron temperatures considered in the spectral fitting routine. Higher-charge states of Al are ionized in succession and absorb in  $1s-2p$  transitions as the shell  $T_e$  increases. At time  $t = 0$  ns, the laser irradiation of the target begins. When the shock propagates through the buried Al layer, the sharp rise in the temperature ionizes the Al and the lowest-charge states of Al (i.e., F-like and O-like) are observed in  $1s-2p$  absorption. The second rise in electron temperature at 0.75 ns occurs when the heat front penetrates the Al layer and ultimately ionizes it to the K shell. The minimum electron temperature that can be currently diagnosed using this technique is  $\sim 10$  eV.

Time-resolved x-ray absorption spectroscopy was performed using a  $50\text{-}\mu\text{m}$ -thick target with a 1- or  $2\text{-}\mu\text{m}$ -thick Al layer buried at a depth of  $10\text{ }\mu\text{m}$ . Two laser intensities were studied:  $1 \times 10^{14}$  W/cm<sup>2</sup> generating a 10-Mbar shock and  $1 \times 10^{15}$  W/cm<sup>2</sup> generating a 50-Mbar shock. The predicted, shocked mass density in the Al layer for the higher intensity drive is  $\sim 8$  g/cm<sup>3</sup>. The streaked x-ray spectra are presented in Fig. 109.12 with the prominent absorption features identified. The cold K edge of Al can be observed prior to the shock arrival at the Al layer. The diagnostic utility of the temperature and density dependence of the K-edge shift is currently being studied. Only the F-like Al  $1s-2p$  absorption feature is observed with the lower drive intensity [Fig. 109.12(a)]. The three lowest-charge states (F-like, O-like, and N-like) appear in absorption when shock heated by the higher intensity [Fig. 109.12(b)]. The Sm backlighter and the CH/Al/CH target have the same 1-ns square laser pulse drive, but the Sm backlighter was fired 200 ps earlier than the drive foil to optimize the backlighter brightness for the shock-heating period of the Al layer. The higher charge states associated with the heat-front penetration that are predicted in Fig. 109.11 are not observed in Fig. 109.12(b) because the Sm backlighter was off at that time. The temporal onset of the  $1s-2p$  absorption depends on the buried depth of the Al layer and the shock velocity.

The measured spectral line shapes were compared with simulated absorption spectra calculated with *LILAC* and *Spect3D*.

A detailed description can be found elsewhere.<sup>37</sup> Reasonable agreement was observed for the lower drive intensity; however, the higher-charge states were observed in the measured absorption spectrum compared to the simulated absorption spectrum for the higher drive intensity. This indicates that the measured electron temperature is higher than the prediction. The measured spectra were compared with simulated spectra calculated with PrismSPECT<sup>52</sup> assuming uniform shell conditions for various combinations of  $n_e$  and  $T_e$ . The best fit to the measured spectra was determined based on a least-squares-fitting routine, which inferred  $n_e$  and  $T_e$  simultaneously. The electron density inferred from the higher laser drive intensity was  $1 \times 10^{24} \text{ cm}^{-3}$

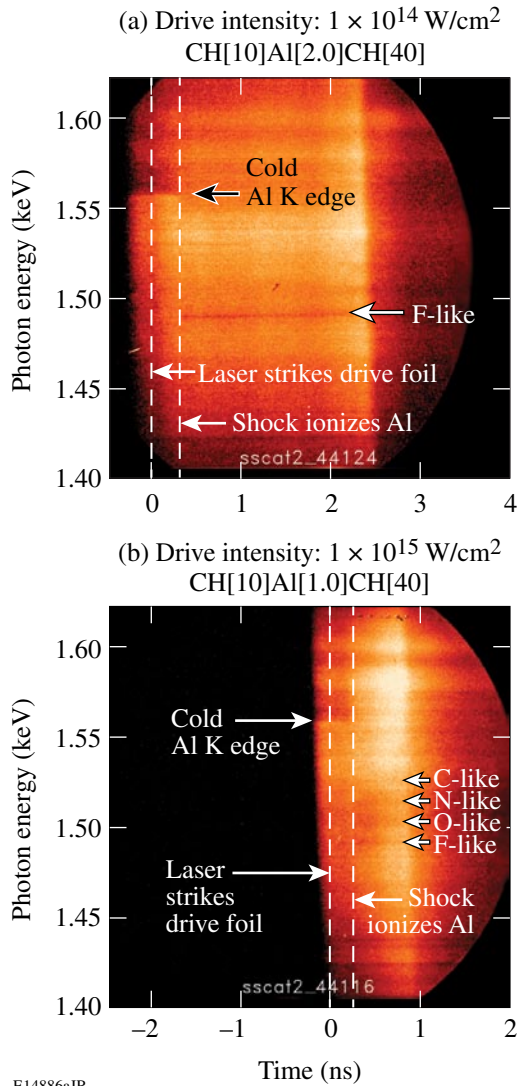


Figure 109.12 Time-resolved x-ray absorption spectra recorded for drive intensities of (a)  $1 \times 10^{14} \text{ W/cm}^2$  and (b)  $1 \times 10^{15} \text{ W/cm}^2$ . The prominent absorption features are identified.

and for the lower drive intensity was  $5 \times 10^{23} \text{ cm}^{-3}$ , consistent with the 1-D predictions. The time history comparing the predicted electron temperature with the measurements is shown in Fig. 109.13. Again, the simulated electron temperature was calculated as follows: (1) LILAC was post-processed with Spect3D and (2) the simulated absorption spectra were fitted with PrismSPECT, assuming uniform electron temperature and density in the Al layer. These calculations were performed

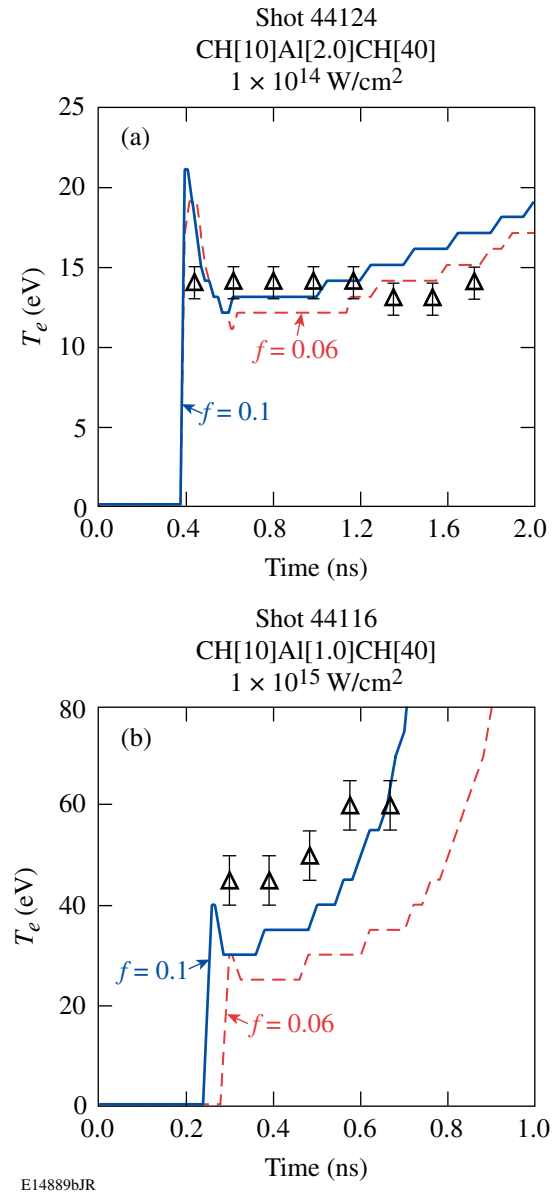


Figure 109.13 Comparison of time-resolved electron temperature in the Al layer inferred from the experiment (triangles) with LILAC simulations using  $f = 0.06$  (dashed curves) and  $f = 0.1$  (solid curves) for drive intensities of (a)  $1 \times 10^{14} \text{ W/cm}^2$  and (b)  $1 \times 10^{15} \text{ W/cm}^2$ .

for two flux limiters ( $f = 0.06$  and  $f = 0.1$ ). For the lower drive intensity the predicted electron temperatures for both flux limiters are close to the time-resolved electron temperatures inferred from the measured absorption spectra [Fig. 109.13(a)]. These experimental measurements are consistent with the results from the noncollective spectrally resolved x-ray scattering experiment of a similar drive foil: an upper limit of  $T_e = 20$  eV was inferred in those experiments.<sup>38</sup> The time-resolved electron temperatures inferred from the measured absorption spectra are higher than the simulated ones for the  $1 \times 10^{15}$  W/cm<sup>2</sup> drive intensity [Fig. 109.13(b)]. The simulation with the higher flux limiter predicts more shock heating and an earlier penetration of the heat front. The initial level of measured shock heating is higher than the simulation with  $f = 0.1$ ; however, the timing of the heat-front penetration is similar.

### Discussion

The experimental results indicate that the energy transport from the critical density to the ablation front cannot be described by flux-limited diffusion and may be nonlocal. The role of nonlocal thermal transport is twofold: (1) It results in an effective time-dependent flux limiter that influences the laser absorption fraction, the shock timing, and the shock-heated conditions. (2) It results in preheat through the transport of energetic electrons, which would increase the shell temperature. All of the experimental results presented in this article were compared with *LILAC* simulations having flux limiters of  $f = 0.06$  and  $f = 0.1$ . The measurements are accurate enough to distinguish between these two models. In some cases the simulations with the higher flux limiter were closer to the experimental observables. A higher flux limiter was needed to reduce the discrepancies between the simulations and measurements for the early-time laser absorption, the mass ablation rate with laser irradiation of  $1 \times 10^{15}$  W/cm<sup>2</sup>, and the shock heating with laser irradiation of  $1 \times 10^{15}$  W/cm<sup>2</sup>. Preheat due to energetic electrons and x rays from the corona may explain shock heating at laser irradiation of  $1 \times 10^{15}$  W/cm<sup>2</sup>. These observations are consistent with the effects of nonlocal electron thermal transport.<sup>39</sup> Other effects influencing the measurements also need to be investigated. The higher early-time laser absorption may be caused by resonance absorption,<sup>54</sup> which is not included in the *LILAC* prediction. *LILAC* may be underestimating the predicted electron temperature due to shock heating. The accuracy of modeling the electron temperature in the Al layer needs to be investigated. The simulations with the lower flux limiter of  $f = 0.06$  were close to the measurements of shock heating at laser irradiation of  $1 \times 10^{14}$  W/cm<sup>2</sup>. This could be consistent with a nonlocal electron thermal transport if the preheat is negligible at the lower intensity.

This detailed comparison of the results from the experiment and *LILAC* reveals the limitations of a flux-limited thermal-transport model for direct-drive ICF: a single-flux limiter cannot explain all the experimental observables. Laser absorption measurements indicate a time-dependent flux limiter is required. However, a nonlocal treatment of the thermal transport currently under development<sup>39</sup> is expected to improve agreement between the simulations and the experimental results.

### Conclusion

An investigation of direct-drive energy coupling was conducted to tune the physics models of the 1-D hydrodynamics code *LILAC*. The flow of energy from the laser to the target was inferred by measuring the laser absorption fraction, the mass ablation rate, and the amount of shock heating. The highly reproducible experimental results achieved with a high level of laser drive uniformity constrain the modeling of direct-drive energy coupling. All of the experimental results were compared with *LILAC* simulations having flux limiters of  $f = 0.06$  and  $f = 0.1$ . The detailed comparison reveals the limitation of a flux-limited thermal-transport model for direct-drive ICF: a single-flux limiter cannot explain all the experimental observables. Furthermore, simulations of laser absorption measurements need a time-dependent flux limiter to match the data. The experimental results indicate that the energy transport from the critical density to the ablation front is probably nonlocal. A nonlocal treatment of the thermal transport in *LILAC* is expected to improve the agreement between the simulations and the experimental results.

### ACKNOWLEDGMENT

This work was supported by the U.S. Department of Energy Office of Inertial Confinement Fusion under Cooperative Agreement No. DE-FC52-92SF19460, the University of Rochester, and the New York State Energy Research and Development Authority. The support of DOE does not constitute an endorsement by DOE of the views expressed in this article.

### REFERENCES

1. J. Nuckolls *et al.*, *Nature* **239**, 139 (1972).
2. J. D. Lindl, R. L. McCrory, and E. M. Campbell, *Phys. Today* **45**, 32 (1992).
3. R. L. McCrory, J. M. Soures, C. P. Verdon, F. J. Marshall, S. A. Letzring, S. Skupsky, T. J. Kessler, R. L. Kremens, J. P. Knauer, H. Kim, J. Delettrez, R. L. Keck, and D. K. Bradley, *Nature* **335**, 225 (1988).
4. J. D. Lindl, *Inertial Confinement Fusion: The Quest for Ignition and Energy Gain Using Indirect Drive* (Springer-Verlag, New York, 1998).
5. S. E. Bodner, D. G. Colombant, J. H. Gardner, R. H. Lehmburg, S. P. Obenschain, L. Phillips, A. J. Schmitt, J. D. Sethian, R. L. McCrory, W. Seka, C. P. Verdon, J. P. Knauer, B. B. Afeyan, and H. T. Powell, *Phys. Plasmas* **5**, 1901 (1998).

6. P. W. McKenty, V. N. Goncharov, R. P. J. Town, S. Skupsky, R. Betti, and R. L. McCrory, *Phys. Plasmas* **8**, 2315 (2001).
7. J. D. Lindl *et al.*, *Phys. Plasmas* **11**, 339 (2004).
8. P. W. McKenty, T. C. Sangster, M. Alexander, R. Betti, R. S. Craxton, J. A. Delettrez, L. Elasky, R. Epstein, A. Frank, V. Yu. Glebov, V. N. Goncharov, D. R. Harding, S. Jin, J. P. Knauer, R. L. Keck, S. J. Loucks, L. D. Lund, R. L. McCrory, F. J. Marshall, D. D. Meyerhofer, S. P. Regan, P. B. Radha, S. Roberts, W. Seka, S. Skupsky, V. A. Smalyuk, J. M. Soures, K. A. Thorp, M. Wozniak, J. A. Frenje, C. K. Li, R. D. Petrasso, F. H. Séguin, K. A. Fletcher, S. Padalino, C. Freeman, N. Izumi, J. A. Koch, R. A. Lerche, M. J. Moran, T. W. Phillips, G. J. Schmid, and C. Sorce, *Phys. Plasmas* **11**, 2790 (2004).
9. R. L. McCrory, S. P. Regan, S. J. Loucks, D. D. Meyerhofer, S. Skupsky, R. Betti, T. R. Boehly, R. S. Craxton, T. J. B. Collins, J. A. Delettrez, D. Edgell, R. Epstein, K. A. Fletcher, C. Freeman, J. A. Frenje, V. Yu. Glebov, V. N. Goncharov, D. R. Harding, I. V. Igumenshchev, R. L. Keck, J. D. Kilkenny, J. P. Knauer, C. K. Li, J. Marciante, J. A. Marozas, F. J. Marshall, A. V. Maximov, P. W. McKenty, J. Myatt, S. Padalino, R. D. Petrasso, P. B. Radha, T. C. Sangster, F. H. Séguin, W. Seka, V. A. Smalyuk, J. M. Soures, C. Stoeckl, B. Yaakobi, and J. D. Zuegel, *Nucl. Fusion* **45**, S283 (2005).
10. R. Betti, K. Anderson, T. R. Boehly, T. J. B. Collins, R. S. Craxton, J. A. Delettrez, D. H. Edgell, R. Epstein, V. Yu. Glebov, V. N. Goncharov, D. R. Harding, R. L. Keck, J. H. Kelly, J. P. Knauer, S. J. Loucks, J. A. Marozas, F. J. Marshall, A. V. Maximov, D. N. Maywar, R. L. McCrory, P. W. McKenty, D. D. Meyerhofer, J. Myatt, P. B. Radha, S. P. Regan, C. Ren, T. C. Sangster, W. Seka, S. Skupsky, A. A. Solodov, V. A. Smalyuk, J. M. Soures, C. Stoeckl, W. Theobald, B. Yaakobi, C. Zhou, J. D. Zuegel, J. A. Frenje, C. K. Li, R. D. Petrasso, and F. H. Séguin, *Plasma Phys. Control. Fusion* **48**, B153 (2006).
11. M. C. Herrmann, M. Tabak, and J. D. Lindl, *Nucl. Fusion* **41**, 99 (2001).
12. R. Betti, K. Anderson, V. N. Goncharov, R. L. McCrory, D. D. Meyerhofer, S. Skupsky, and R. P. J. Town, *Phys. Plasmas* **9**, 2277 (2002).
13. T. R. Boehly, D. L. Brown, R. S. Craxton, R. L. Keck, J. P. Knauer, J. H. Kelly, T. J. Kessler, S. A. Kumpan, S. J. Loucks, S. A. Letzring, F. J. Marshall, R. L. McCrory, S. F. B. Morse, W. Seka, J. M. Soures, and C. P. Verdon, *Opt. Commun.* **133**, 495 (1997).
14. S. P. Regan, J. A. Marozas, R. S. Craxton, J. H. Kelly, W. R. Donaldson, P. A. Jaanimagi, D. Jacobs-Perkins, R. L. Keck, T. J. Kessler, D. D. Meyerhofer, T. C. Sangster, W. Seka, V. A. Smalyuk, S. Skupsky, and J. D. Zuegel, *J. Opt. Soc. Am. B* **22**, 998 (2005).
15. J. Delettrez, R. Epstein, M. C. Richardson, P. A. Jaanimagi, and B. L. Henke, *Phys. Rev. A* **36**, 3926 (1987); J. Delettrez, *Can. J. Phys.* **64**, 932 (1986).
16. J. Paisner *et al.*, *Laser Focus World* **30**, 75 (1994).
17. P. B. Radha, V. N. Goncharov, T. J. B. Collins, J. A. Delettrez, Y. Elbaz, V. Yu. Glebov, R. L. Keck, D. E. Keller, J. P. Knauer, J. A. Marozas, F. J. Marshall, P. W. McKenty, D. D. Meyerhofer, S. P. Regan, T. C. Sangster, D. Shvarts, S. Skupsky, Y. Srebro, R. P. J. Town, and C. Stoeckl, *Phys. Plasmas* **12**, 032702 (2005).
18. H. Takabe *et al.*, *Phys. Fluids* **28**, 3676 (1985).
19. R. Betti, V. N. Goncharov, R. L. McCrory, and C. P. Verdon, *Phys. Plasmas* **5**, 1446 (1998).
20. S. P. Regan, J. A. Delettrez, V. N. Goncharov, F. J. Marshall, J. M. Soures, V. A. Smalyuk, P. B. Radha, B. Yaakobi, R. Epstein, V. Yu. Glebov, P. A. Jaanimagi, D. D. Meyerhofer, T. C. Sangster, W. Seka, S. Skupsky, C. Stoeckl, D. A. Haynes, Jr., J. A. Frenje, C. K. Li, R. D. Petrasso, and F. H. Séguin, *Phys. Rev. Lett.* **92**, 185002 (2004).
21. V. N. Goncharov, J. P. Knauer, P. W. McKenty, P. B. Radha, T. C. Sangster, S. Skupsky, R. Betti, R. L. McCrory, and D. D. Meyerhofer, *Phys. Plasmas* **10**, 1906 (2003).
22. K. Anderson and R. Betti, *Phys. Plasmas* **10**, 4448 (2003).
23. R. C. Malone, R. L. McCrory, and R. L. Morse, *Phys. Rev. Lett.* **34**, 721 (1975).
24. W. Seka, J.-L. Schwob, and C. Breton, *J. Appl. Phys.* **42**, 315 (1971).
25. F. C. Young *et al.*, *Appl. Phys. Lett.* **30**, 45 (1977).
26. B. Yaakobi and T. C. Bristow, *Phys. Rev. Lett.* **38**, 350 (1977).
27. B. H. Ripin *et al.*, *Phys. Fluids* **23**, 1012 (1980).
28. M. H. Key, R. G. Evans, and D. J. Nicholas, Rutherford Appleton Laboratory, Chilton, Didcot, Oxon, England, Report RL-78-020/XAB (1978).
29. B. Yaakobi, T. Boehly, P. Bourke, Y. Conturie, R. S. Craxton, J. Delettrez, J. M. Forsyth, R. D. Frankel, L. M. Goldman, R. L. McCrory, M. C. Richardson, W. Seka, D. Shvarts, and J. M. Soures, *Opt. Commun.* **39**, 175 (1981).
30. T. J. Goldsack *et al.*, *Opt. Commun.* **42**, 55 (1982); T. J. Goldsack *et al.*, *Phys. Fluids* **25**, 1634 (1982).
31. M. H. Key *et al.*, *Phys. Fluids* **26**, 2011 (1983).
32. A. Hauer *et al.*, *Phys. Rev. Lett.* **53**, 2563 (1984).
33. J. Delettrez, R. Epstein, M. C. Richardson, P. A. Jaanimagi, and B. L. Henke, *Phys. Rev. A* **36**, 3926 (1987).
34. D. K. Bradley, J. A. Delettrez, and C. P. Verdon, *Phys. Rev. Lett.* **68**, 2774 (1992).
35. D. J. Hoarty *et al.*, *J. Quant. Spectrosc. Radiat. Transf.* **99**, 283 (2006).
36. T. R. Boehly, J. A. Delettrez, J. P. Knauer, D. D. Meyerhofer, B. Yaakobi, R. P. J. Town, and D. Hoarty, *Phys. Rev. Lett.* **87**, 145003 (2001).
37. H. Sawada, S. P. Regan, R. Epstein, D. Li, V. N. Goncharov, P. B. Radha, D. D. Meyerhofer, T. R. Boehly, V. A. Smalyuk, T. C. Sangster, B. Yaakobi, and R. C. Mancini, "Investigation of Direct-Drive Shock Heating Using XRay Absorption Spectroscopy," to be submitted to *Physics of Plasmas*.
38. H. Sawada, S. P. Regan, D. D. Meyerhofer, I. V. Igumenshchev, V. N. Goncharov, T. R. Boehly, T. C. Sangster, V. A. Smalyuk, B. Yaakobi, G. Gregori, S. H. Glenzer, and O. L. Landen, "Diagnosing Direct-Drive, Shock-Heated Plastic Planar Foils with Noncollective Spectrally Resolved X-Ray Scattering," to be submitted to *Physics of Plasmas*.

39. V. N. Goncharov, O. V. Gotchev, E. Vianello, T. R. Boehly, J. P. Knauer, P. W. McKenty, P. B. Radha, S. P. Regan, T. C. Sangster, S. Skupsky, V. A. Smalyuk, R. Betti, R. L. McCrory, D. D. Meyerhofer, and C. Cherfils-Clérouin, *Phys. Plasmas* **13**, 012702 (2006).
40. A. R. Bell, R. G. Evans, and D. J. Nicholas, *Phys. Rev. Lett.* **46**, 243 (1981).
41. W. F. Huebner *et al.*, Los Alamos National Laboratory, Los Alamos, NM, Report LA-6760-M (1977).
42. L. Spitzer, Jr. and R. Härm, *Phys. Rev.* **89**, 977 (1953).
43. A. Sunahara, J. A. Delettrez, C. Stoeckl, R. W. Short, and S. Skupsky, *Phys. Rev. Lett.* **91**, 095003 (2003).
44. W. Seka, L. M. Goldman, M. C. Richardson, J. M. Soures, K. Tanaka, B. Yaakobi, R. S. Craxton, R. L. McCrory, R. Short, E. A. Williams, T. Boehly, R. Keck, and R. Boni, in *Plasma Physics and Controlled Nuclear Fusion Research 1982* (IAEA, Vienna, 1983), Vol. I, pp. 131–137.
45. J. M. Soures, T. C. Bristow, H. Deckman, J. Delettrez, A. Entenberg, W. Friedman, J. Forsyth, Y. Gazit, G. Halpern, F. Kalk, S. Letzring, R. McCrory, D. Peiffer, J. Rizzo, W. Seka, S. Skupsky, E. Thorsos, B. Yaakobi, and T. Yamanaka, in *Laser Interaction and Related Plasma Phenomena*, edited by H. J. Schwarz, H. Hora, M. J. Lubin, and B. Yaakobi (Plenum Press, New York, 1981), Vol. 5, pp. 463–481.
46. W. Seka, R. S. Craxton, J. Delettrez, L. Goldman, R. Keck, R. L. McCrory, D. Shvarts, J. M. Soures, and R. Boni, *Opt. Commun.* **40**, 437 (1982).
47. M. C. Richardson, R. S. Craxton, J. Delettrez, R. L. Keck, R. L. McCrory, W. Seka, and J. M. Soures, *Phys. Rev. Lett.* **54**, 1656 (1985).
48. W. Seka, V. N. Goncharov, J. A. Delettrez, D. H. Edgell, I. V. Igumenshchev, R. W. Short, A. V. Maximov, J. Myatt, and R. S. Craxton, “Time-Dependent Absorption Measurements in Direct-Drive Spherical Implosions,” to be submitted to *Physics of Plasmas*.
49. S. P. Regan, D. K. Bradley, A. V. Chirikikh, R. S. Craxton, D. D. Meyerhofer, W. Seka, R. W. Short, A. Simon, R. P. J. Town, B. Yaakobi, J. J. Carroll III, and R. P. Drake, *Phys. Plasmas* **6**, 2072 (1999).
50. T. R. Boehly, E. Vianello, J. E. Miller, R. S. Craxton, T. J. B. Collins, V. N. Goncharov, I. V. Igumenshchev, D. D. Meyerhofer, D. G. Hicks, P. M. Celliers, and G. W. Collins, *Phys. Plasmas* **13**, 056303 (2006).
51. D. H. Kalantar *et al.*, in *22nd International Congress on High-Speed Photography and Photonics*, edited by D. L. Paisley and A. M. Frank (SPIE, Bellingham, WA, 1997), Vol. 2869, pp. 680–685.
52. Prism Computational Sciences, Inc., Madison, WI 53711.
53. O. Gotchev, V. N. Goncharov, J. P. Knauer, T. R. Boehly, T. J. B. Collins, R. Epstein, P. A. Jaanimagi, and D. D. Meyerhofer, *Phys. Rev. Lett.* **96**, 115005 (2006).
54. W. L. Kruer, *The Physics of Laser-Plasma Interactions, Frontiers in Physics*, Vol. 73, edited by D. Pines (Addison-Wesley, Redwood City, CA, 1988).